Research Article | Vol. 28, No. 9 / 27 April 2020 / Optics Express 13845
Optics EXPRESS

Optically-thick 300 nm GaAs solar cells using adjacent photonic crystals

JERONIMO BUENCUERPO,* MYLES A. STEINER, AND ADELE C. TAMBOLI

National Renewable Energy Laboratory, Golden, CO 80401, USA
jeronimo.buencuerpo@nrel.gov

Abstract: Ultra-thin photovoltaics offer the potential for increasing efficiency while minimizing costs. However, a suitable light trapping strategy is needed to reach the optically thick regime for otherwise thin-film structures. III-V materials can benefit from simple adjacent light trapping structures, if correctly designed. Here we present three strategies for a 300 nm thick GaAs cell using front photonic crystals, back photonic crystals, and both front and back combined, predicting a maximum photocurrent, J_{sc}=29.9 mA/cm^2 under the radiative limit, including an enhanced absorption in the Urbach-tail. We analyze the increased absorption isolating the Fabry-Perot resonances, the single pass absorption and the scattered contribution from the incident light.

1. Introduction

III-V materials present the highest efficiency solar cells, consistently dominating the record efficiency tables for both single junction and multijunction devices [1]. Multijunction III-V based materials are standard for space applications due to their high efficiency, power per mass and area, and better radiation hardness than, for example, silicon. Nevertheless, the production cost has limited the terrestrial applications of these materials. Meanwhile, Si costs have dropped, dominating the terrestrial applications [2], but the efficiency of silicon is reaching its limit [3], and is lower than GaAs cells. Both cost and efficiency drive photovoltaics adoption: to surpass Si, new options have emerged, such as thin films and hybrid multijunctions on Si [4–6]. In this work, we have centered our optimization efforts on a single GaAs junction, but the design concepts are applicable for other thin films and hybrid tandems. There are three main open fronts to minimize the cost of the III-V based photovoltaics: reusable substrates, materials, and deposition time [7]. Reducing the thickness of the solar cell directly reduces materials used and deposition time. In addition, thinner devices are preferable for space applications where radiation degradation scales with thickness [8–10], and it may open the door for cheaper but lower quality growths [11–13].

Advanced optical engineering of thin cells has been done in the past, with theoretical and experimental results in the literature [14–25]. In particular for III-V nanostructures, the fundamental idea is to do the nanostructuring it outside of the active layer to avoid degradation of the device quality due to increased surface recombination. This rule was applied for layers on the upper front of the cell [15,16,19], the back [18,20], or front and back [21,22]. Nanostructuring outside of the III-V solar cell is fundamental to achieve better experimental results, and it is usually neglected in the numerical calculus literature. Furthermore, III-V materials present a different behavior and challenges than other materials because of their high extinction coefficient and the use of ultrathin layers of hundreds of nm limiting the waveguiding. Also, the main objective of thin GaAs cells is to match or improve the already high efficiency of thicker III-V cells. If the design presented is not able to reach the photocurrent (J_{sc}) of thick devices, typically around 30 mA/cm^2, the usefulness of the fabricated structures will fail in comparison with their thick counterparts, and the justification for adding the nanostructuring process may limit their applications. Therefore, the light trapping structures must be carefully designed and optimized.

#391737 https://doi.org/10.1364/OE.391737
Journal © 2020 Received 5 Mar 2020; revised 9 Apr 2020; accepted 9 Apr 2020; published 22 Apr 2020
Corrected: 24 April 2020

Optics EXPRESS

The objective of this work is to demonstrate that a GaAs cell with only a few hundred nm, in the ultra-thin regime, can be effectively optically thick using adjacent nanostructured layers. We place these layers at the front and the back of the cell. We follow simple design rules prior to an optimization. First, these nanostructured layers are made of transparent materials for the useful spectrum, dielectrics on top layers (full solar spectrum) and high-bandgap semiconductors for the bottom layers (solar spectrum filtered by the upper cell). Second, we use simple motifs, nanostructured photonic crystals to diffract light into different non-normal optical modes in the semiconductor. And finally, we add a dielectric spacer between these nanostructured layers and the back metal mirror to avoid parasitic absorption in the metal. These rules can be applied to ultra-thin GaAs cells that can obtain J_{sc} close to 30 mA/cm^2, competitive with thick cells, and can also be extended to other type of ultrathin cells. The scheme of this design is shown in Fig. 1(a), and is detailed in the design section.

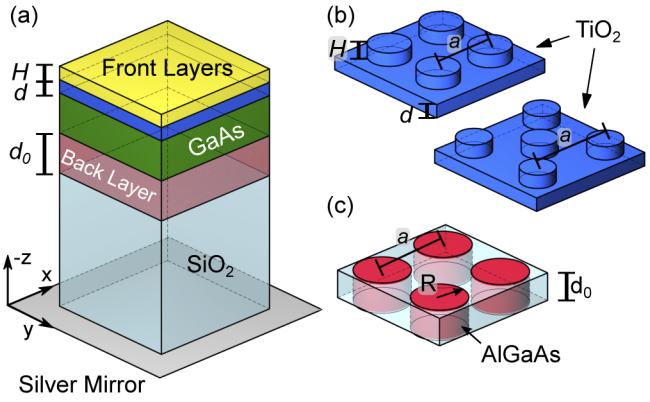

Fig. 1. (a) Optical stack used for the cases studied. (b) Front PC made of TiO_2 cylinders, with with lattice parameter a in a square lattice, when using it alone, and two square lattices displaced $(a/2, a/2)$ when combined with a back PC. The cylinders have height H and radius R. (c) Scheme of back PC with cylinders of AlGaAs in SiO_2 with square lattice a. The height of the cylinders is d_0

2. Design

To test the design rules we optimize the thinnest absorber that can obtain a comparable J_{sc} to a thick device. We establish the thinnest absorber from an optical point of view, using a Lambertian absorber [26], and under the radiative limit. In the limit of a thin layer with ideal Lambertian surfaces, a 300 nm GaAs layer can generate 98% of the available J_{sc} (30.3 mA/cm^2 vs. 31.0 mA/cm^2) . We adopt this thickness as a target for our optical design and seek structures that can achieve similar J_{sc}. We have included reflection losses using the reflection of a thick (3μm) absorber using a double layer ARC of MgF_2 (100 nm) and TiO_2 (50 nm) to be more realistic.

One key aspect is choosing the materials for the scatterers, which need to be transparent for the wavelength range of operation. In this paper, we calculate and optimize photonic crystals (PC) in the front and back of the active layer. Naively, the design should be based on materials completely transparent in the range of interest between the semiconductor bandgap and the UV, where solar radiation drops off. Using entirely transparent materials is fundamental for the front photonic crystal material, as it will filter the incoming light towards the solar cell. We choose TiO_2 with an absorption edge in the UV. However, this is not true when we are placing the nanostructure in the back of the solar cell, as the upper layers filter the spectrum, allowing the use of semiconductors instead of dielectrics. The main advantage of choosing semiconductors is that their refractive index is larger than for dielectrics, resulting in enhanced scattering efficiency

Optics EXPRESS

and light confinement. We choose III-V materials due to their band-gap and lattice constant tunability. It has been proposed to use a III-V as back semiconductor photonic crystals, using GaInP [10], AlInP [14], and recently AlGaAs [27]. In particular, as we are designing a GaAs cell, we choose AlGaAs and vary the aluminum content, which will negligibly modify the lattice constant. However, it will strongly modify the absorption edge. To minimize the parasitic absorption for the 300 nm absorber, we require an Al_xGa_{1-x} As with an aluminum content of at least 70%. The overall cell structure is assumed to be in an air/vacuum medium with a back reflector, a silver mirror. We place a dielectric spacer between the cell (SiO_2, 1μm thick) and the mirror to avoid coupling to the surface plasmon polariton by frustrated reflection [28,29]. The optical stack is placed in parallel x-y planes, see Fig. 1(a). We assume a real device will have a typical design for III-V cells with metallic fingers as feed-through, in our case on both sides, with spacings of several hundred microns [17,27]. These fingers grids are microns in diameter and lead to a constant shadow loss of 3-5% in all devices

Once we have defined our materials and layers, we can choose the type of photonic crystal that we are going to use. We choose fairly simple photonic crystals, cylinders in a square lattice. These motifs can be produced by nanoimprint [17,30] or laser interference lithography [30]. We study three different cases: the front PC, the back PC, and a final case combining the front and back PC. The photonic crystals are defined by its lattice parameter a, its radius R. The thickness of the nanostructured layer, is H when we place it in the front, and d_0 when we place it in the back, see Figs. 1(a)–(c). We have included an additional layer of TiO_2, with thickness d, between the front layer and the GaAs cell. The front PC is made of TiO_2, see Fig. 1(b). When using only the front PC, the layer d_0 is a planar SiO_2 layer. The back PC is made of $Al_{0.70}Ga_{0.30}$ As embedded in SiO_2, see Fig. 1(c). When using the back PC, the front layer H is a planar MgF_2 layer, creating a double layer ARC with the layer d. Finally, when we use both photonic crystals layers, we have to force one unique unit cell between the front and back PC. Also, we have two different radius, front (R_f) and back (R_b). We impose a smaller sub-lattice on the front photonic crystal using two square lattices displaced, face and a square lattice for the bottom, see Fig. 1(b). Choosing a smaller lattice for the front makes sense intuitively because it should minimize the diffraction orders in the incident medium, and it is also found in the literature when developing nanostructured ARCs [21,30–32]. The challenge of fabricating a front nanostructured dielectric has been addressed experimentally [30,32], and also, creating back embedded nanostructures in SiO_2 [17,27]. An optimized design and understanding of the absorption processes involved is needed to push forward the efficiency of ultrathin GaAs cells.

For each case, we optimize all the parameters at the same time a, H, d, d_0 and its radius (R or, R_f and R_b if using the front and back PC). The optimization is done in two steps by combining local and global optimizations [33]. Initially, we do 3000 steps using a controlled random search with global mutation [34], and then 1000 optimization steps using a local bound optimization around the rough global maximum a higher amount [35]. In both cases, global and local, all the parameters of each nanostructure is optimized at the same time.

3. Theory

We use rigorous coupled-wave analysis (RCWA) to model the structure [36]. The refractive indices are obtained from [37–40]. To calculate the absorption $A(\lambda)$ for each wavelength, one starts by computing the power flux

$$P(\lambda, z) = \iint_{\text{u.c.}} <S(\lambda, x, y, z)> \hat{n}\, dx\, dy; \tag{1}$$

where $<S>$ is the time-average Poynting vector, $\hat{n}$ is the surface normal unit vector, a^2 is the unit cell area (u.c.), with a as lattice parameter, and z is the normal axis. The absorption between the layer placed at $z = z_i$ and $z = z_{i+1}$ is simply the difference in power flux $A(\lambda) = P(\lambda, z_i) - P(\lambda, z_{i+1})$.

Optics EXPRESS

The absorption can also be calculated locally, $A(\lambda, z)$, for a z using an infinitesimal layer. For simplicity, we use the following derivation for time-averaged magnitudes S and E^2. Hence, the angle bracket notation is dropped out. Using the Bragg harmonics, we study the coupling of the incoming light with wavevector, $\mathbf{k} = (k_x, k_y, k_z)$ and wavelength λ_0 with the PC with reciprocal square lattice unit vector $\mathbf{g}$:

$$k_{x,y}^2 \equiv k_p^2 = \left(k_x + \frac{2\pi}{a} g_x\right)^2 + \left(k_y + \frac{2\pi}{a} g_y\right)^2, \tag{2}$$

$$k_z = \sqrt{\frac{2\pi\varepsilon_a}{\lambda_0} - k_p^2}; \tag{3}$$

$$\mathbf{g} = (g_x, g_y); g_{x,y} = 0, \pm 1, \pm 2, \ldots. \tag{4}$$

where k_p is the parallel projection, and ε_a is the dielectric permittivity of the layer, GaAs in our case. The k_p component appears because the momentum transfer from the PC lattice to the incident wave [41]. The physical implication of light with k_p, partially flowing parallel, is the appearance of quasi-guided modes inside the optical stack [41,42]. Active layers with weak absorption benefit from these modes for increasing the absorptance.

Using the Fourier series that reconstruct the fields in rigorous coupled wave analysis (RCWA), for the homogeneous GaAs layer we study the power flux, P:

$$P(\lambda, z) = P(\lambda, z, g = 0) + P(\lambda, z, g{>}0), \tag{5}$$

where $P(\lambda, z, g = 0)$ represents the light in the zero diffraction order, namely keeping is original wavevector, therefore, non-scattered; and $P(\lambda, z, g{>}0)$ the light sum of all the non-zero diffraction orders, namely with a changed wavevector, therefore, scattered.

By using this distinction, we identify the absorption by harmonics $g{>}0$ as the absorption by light scattered,

$$A(\lambda)_{g>0} = P(\lambda, z_i)_{g>0} - P(\lambda, z_{i+1})_{g>0}, \tag{6}$$

for the layer between z_i and z_{i+1}, and analogously for the zeroth-order, $g = 0$. Indeed, we can split the scattered contributions in the absorption for the incremental values of g, $A(\lambda)_{g=1,2,\ldots}$, as each family of g it is associated with different propagation,i.e. k. Finally, When k_z is purely real, the wave is propagating in the medium, and we can associate a propagating diffracted angle, θ_d:

$$\theta_d(\lambda, \mathbf{g}) = \sin^{-1}\left(\frac{\lambda_0}{a}\sqrt{\frac{g_x^2 + g_y^2}{\varepsilon_a}}\right). \tag{7}$$

We will use the θ_d to describe the confinement inside the GaAs slab when decomposing the absorption for the different diffraction orders. We will approximate $\varepsilon_a = \Re\{\varepsilon_a\}$ when we are studying the propagation in a lossy medium as the GaAs. This approximation holds when the real part is the major contribution to the impedance between media. For the GaAs, the upper limit is close to 500 nm.

In addition to the absorption and flux analysis, it is interesting to study the light propagation within the structure including the nanostructured layers. Studying the flow of the light inside the photonic structure can be done studying the square of the electric field, E^2, or the electromagnetic energy U. Both can be used to study the space localization for optical resonances [43]. However, the local Poynting vector $\mathbf{S}(\lambda, x, y, x)$ can give us more information about the direction where the power is flowing. We will use the norm of the $|\mathbf{S}|$, which is proportional to E^2 [44], and we can integrate it without losing the information of the parallel propagation, as in Eq. (5). As we are using the planewave expansion, we fix the analysis for a $\lambda = \lambda_i$. Therefore, we drop λ from the

Optics EXPRESS

notation, nevertheless its dependence is buried in **S**. We define the power profile integrating over the unit cell as:

$$W_S(z) \equiv \iint_{\text{u.c.}} S(x, y, z)\, dx\, dy, \tag{8}$$

to obtain the power concentrated at each z. Analogously to the Bragg harmonics decomposition with k, we decompose **S**. We split the vector for parallel and non-parallel contributions to distinguish the amount of power (light) in the parallel components,

$$S^2 = S_p^2 + S_z^2, \tag{9}$$

$$S_p \equiv \sqrt{S_x^2 + S_y^2}. \tag{10}$$

We are interested in the light with high parallel component, S_p, because it implies light (power) flowing mainly in the $x - y$ plane, parallel to the stack layers. Ideally, light modes traveling completely in the $x - y$ plane or under a waveguiding condition (with angles θ_d higher than the critial angle) are confined. Therefore, light can be completely absorbed even under weak absorption limits. However, the modes we obtain from an open system (excited from outside of the stack) will be leaky, and cannot be not purely confined [41]. By studying the amount of power on the parallel component of S_p we can observe the partial confinement of the mode and explain the absorption profile inside the stack, $A(z)$. Finally, we obtain a analogous power profile by integrating S_p over the unit cell:

$$W_{S_p}(z) = \iint_{\text{u.c.}} S_p(x, y, z)\, dx\, dy. \tag{11}$$

The difference between the two energies, W_S and W_{S_p} correspond to the light not entirely confined, namely with a non zero z component,

$$W_{S_{np}} = W_S - W_{S_p}. \tag{12}$$

For clarity, when comparing the power profile, $W_S(z)$ and $A(z)$, we do a feature scaling, a min-max normalization,

$$\widetilde{A}(z) = \frac{A(z) - \min(A(z))}{\max(A(z)) - \min(A(z))}, \tag{13}$$

for the minimum and maximum (min, max) of all the z of the optical stack. We do the same feature scaling for the power $\widetilde{W}_S$. For the power parallel component, W_{S_p}, and the non-parallel component, $W_{S_{np}}$, we normalize to the min-max value of the total W_S, so it is easy to compare,

$$\widetilde{W}_{S_p}(z) = \frac{W_{S_p}(z) - \min(W_S(z))}{\max(W_S(z)) - \min(W_S(z))}, \tag{14}$$

and analogously for the $W_{S_{np}}$.

Finally, the solar cell is modeled in the radiative limit. We use the absorption in the GaAs layer to simulate the quantum efficiency of the device, $A(E) = EQE(E)$. The expected photocurrent assuming complete collection is used as a figure of merit for the optimization [45]:

$$J_{\text{sc}} = (q/hc) \int_0^{\lambda_g} \text{AM1.5g}(\lambda) EQE(\lambda) \lambda \text{d}E, \tag{15}$$

q is the electron charge, h Planck constant, c is the speed of light in vacuum, λ_g the wavelength equals to the band-gap of the GaAs, and AM1.5g(λ) the global spectrum and the absorption in the GaAs layer. Any other absorption in the structure is taken as parasitic and, therefore, as losses.

Optics EXPRESS

4. Results and discussion

The optimal structures are shown in Table 1 and the absorption of the GaAs layer for each structure and their losses (parasitic absorption) are shown in Fig. 2. For comparison, we have included a reference case using a planar double layer ARC (DLARC) MgF_2, and TiO_2 (100 and 50 nm respectively). All the optimized nanostructures obtain absorption near unity for long wavelengths close to the bandgap, obtaining higher absorption than the planar reference structure. The absorption enhancement appears mostly in the long wavelength region, see Figs. 2(a), (c), and (e) black line (total absorption in the GaAs) compared to the thin planar case (gray filled area).

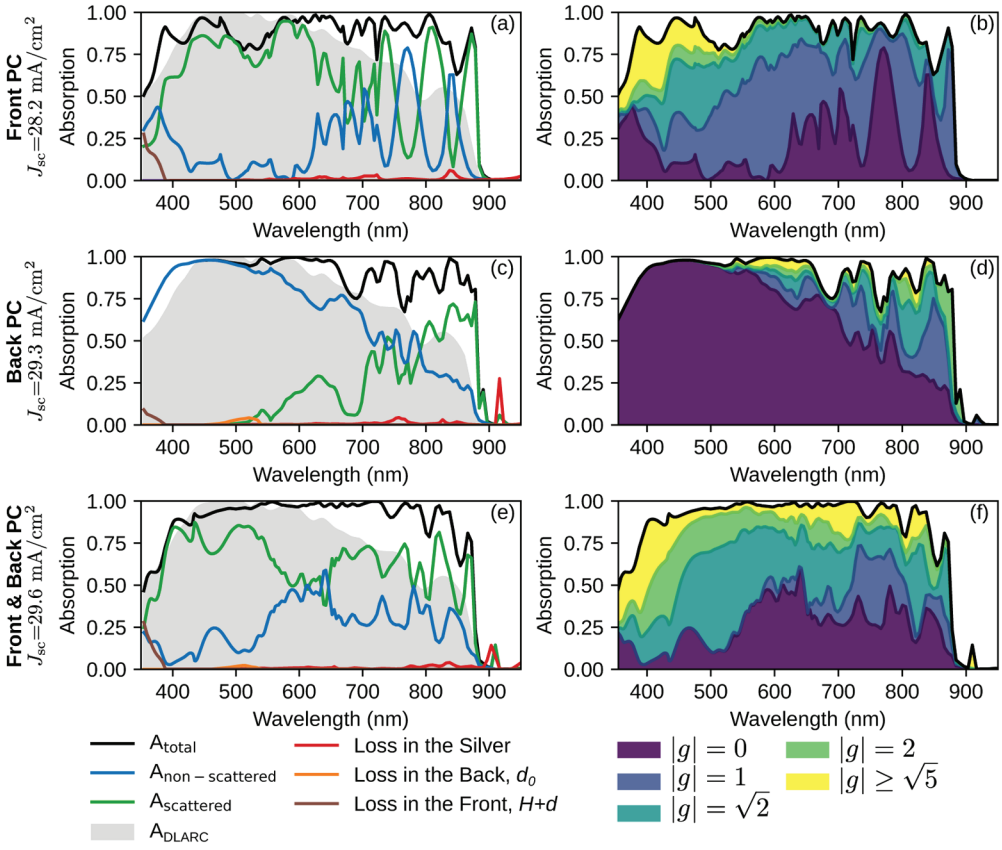

Fig. 2. Left column: absorption and losses for each photonic crystal using Front PC (a), Back PC (c) and Front & Back PC (e). The total absorption for the GaAs layer (black), absorption losses inside the back layer (orange), at the front layer (brown) and at the silver mirror (red). Absorption due to non-scattered light (blue) and scattered light (green). Absorption for the reference without using light trapping layers (fill gray). Right Column: Absorption (black line) and stacked contributions to the absorption for each family of diffraction orders (areas purple to yellow) after expanding the incident wave using the Bragg harmonics in the GaAs cell using front PC (b), back PC (d) and front and back PCs (f).

The thin absorber with a back mirror lacks enough absorption between 700 nm and 900 nm, see Figs. 2(a), (c), and (e). The PC layers should diffract this wavelengths inside the cell stack (GaAs layer and the SiO_2 spacer) to increase the absorption. But, the PC should also minimize the diffraction outside of the structure, i.e. in the air, to minimize the reflection losses [46]. Following the diffraction grating formula under normal incidence, $(a \cdot \sin(\theta_d) = \lambda_0/n)$, the first

Optics EXPRESS

Table 1. Optimum sizes for the nanostructured cases studied

	a (nm)	H (nm)	d (nm)	d_0 (nm)	R (nm)
Front PC	475	196	32	597	142
Back PC	518	85	41	334	201
Front & Back PC	613	149	45	328	R_f=117, R_b=169

diffracted order in the air will appear at a wavelength equal to its value, a, approximately 500 nm. Whereas, the first diffracted order in the rear SiO_2 will appear at $a\, n_{SiO_2} \simeq 750$ nm. The lattice parameter obtained from the optimization are around this 500 nm, see Table 1. The suppression of diffraction orders outside the GaAs layer enhances the confinement of light inside the active slab.

Because of the higher absorption, the nanostructured cases present a higher J_{sc} than the planar case. We calculate the J_{sc} using the absorption obtained. We also include the losses from the added parasitic absorption in the silver mirror, $J_{Ag} = J_{sc}\,(A_{Ag})$, and for the front and back layers as a $J_{p.a.} = J_{sc}\,(A_f + A_b)$. Ideally, the J_{sc} of the structures will be improved if these losses are zero. The J_{sc} values are shown in Table 2, and they are compared with planar DLARC using a 300 nm GaAs absorber and a thick 3μm GaAs solar cell as limiting case. We have included the J_{sc} contributed from the Urbach-tail absorption from 1.35 eV to 1.42 eV, $J_{sc,UT}$. All the nanostructured cases present J_{sc} close to the 30 mA/cm^2 objective. The difference J_{sc} between the front & back PC and the planar thick reference 1.4 mA/cm^2. The radiative limit idealizes the collection and quantum efficiency of the device. For a real device, it is expected the thicker structure will present lower voltage than the thinner one with the same material quaility [12,47]. In that case, the difference between the thick case and the nanostructured thin case will be minimal.

The optical losses of the nanostructured cases are similar to the thin reference, with all the cases having equal or less than 0.5 mA/cm^2 when adding the losses in the silver and at the front and back layers. In comparison with the thick case, the losses in the silver are minimized mainly because a small amount of light reaches the silver mirror in the back. In any case, the spacer and chosen materials minimized these losses. The design achieves the objective of minimizing the parasitic losses on the nanostructured layers and in the back metallic mirror.

When optimizing the structure, we have limited the J_{sc} analysis to a bandgap of 1.42 eV (873 nm) like it is usually done when calculating radiative limits for cells. The absorption does not strictly go to zero in a real material, with the Urbach tail being a low but real absorption below the bandgap. Besides, the Urbach tail absorption gives us information about the enhancement of the absorption for the cell. Typically, a thin absorber does not absorb much in the sub-bandgap region, whereas the thick excels at this range. However, we observe a significant $J_{sc,UT}$ for the nanostructured cases, see Table 2. The back PC presents an enhancement of 0.6 mA/cm^2 close to the limiting case of a thick 3μm absorber with 0.7 mA/cm^2. Allowing to the J_{sc} use the edge of the A (closer to 1.35 eV) instead of arbitrarily cutting down, we would obtain for the back PC a J_{sc}=29.9 mA/cm^2, equivalent to the 29.9 mA/cm^2 for the front and back PC case.

We compare the results with Chen et al. [17], who propose a back periodic nanostructure design with 19.9% efficiency and a J_{sc} of 24.3 mA/cm^2. They present a thin absorber of 205 nm with a roadmap to achieve 25% efficiency solar cells. They propose a back PC made of TiO_2 squares of 420 nm in a square lattice of 700 nm embedded in silver, bigger than the structures presented in this work. The top theoretical efficiency is limited to a 25.6 mA/cm^2 with 2.7 mA/cm^2 of absorption losses in the nanostructured silver mirror. In this work, we are using a transparent semiconductor, opposing to the nanostructuring the silver of the literature, and we are placing a dielectric spacer between the cell and the mirror. This helps lower the optical

Optics EXPRESS

Table 2. J_{sc} for the four thin cases studied, and a planar top limit cell with 3μm absorber. Additional contributions to the J_{sc} from the Urbach-tail, $J_{sc,UT}$. Current losses under the radiative limit because of absorption in the silver mirror, J_{Ag}, and absorption in the non-active layers of the solar cell, $J_{p.a.}$.

	J_{sc} (mA/cm^2)	$J_{sc,UT}$ (mA/cm^2)	J_{Ag} (mA/cm^2)	$J_{p.a.}$ (mA/cm^2)
Planar	25.0	0.1	0.4	0.1
Front PC	28.2	0.5	0.3	0.2
Back PC	29.3	0.6	0.2	0.2
Front & Back PC	29.6	0.3	0.2	0.3
Planar (3μm)	31.0	0.7	0.01	0.1

losses to 0.5 mA/cm^2 and in particular, for the silver losses to 0.2 mA/cm^2 when using a back nanostructure, see Table 2. Also, we propose an absorber of 300 nm combined with the back semiconductor PC to not limit the efficiency below thick devices. The decisions we made about the nanostructured materials, dielectric spacer and minimum thickness allow us to obtain a design with a calculated J_{sc} comparable to a thick device.

4.1. Absorption analysis

Using the decomposition in scattered, $A(\lambda)_{g>0}$, and non-scattered absorption, $A(\lambda)_{g=0}$, we can study the maximum associated for each type of absorption. Using this method, we can identify the kind of peak and propagation at each wavelength. We analyze the absorption in Fig. 2 for the three nanostructured cases.

The front PC case presents an interesting absorption profile for long wavelengths when studying the non-scattered and scattered absorption. The non-scattered light presents two peaks, and two minima, which are easy to associate with the Fabry-Perot (FP) resonances, see Figs. 2(a) and (b). As we have included the back layer d_0 made of SiO_2 in the optimization, the front PC case is tuning the FP resonances from the optical stack to maximize the absorption. The scattered absorption also tunes the absorption with FP resonances but showing an out of phase interval with the non-scattered. This suggests the structure is diffracting the light with a tilted effective angle θ_d. The combination of the FP resonances from the non-scattered contribution and the scattered contribution allows us to obtain a high absorption in the long wavelength region, despite using only a dielectric nanostructure for diffracting. For shorter wavelengths, the amount of diffraction channels available is high, with successive peaks in the absorption, with a minimum at 550 nm. As the cell we optimize is only 300 nm, the front PC has sacrificed some absorption at the short-wavelength to enable a higher absorption near the bandgap and, consequently, higher J_{sc}. Because of this, the lattice parameter of the front PC is higher than the ones found in the literature for optically thick devices [30,32]. The front PC major contribution to the absorption for the range from 400 to 600 nm is from the scattered light. Yet, this range is completely absorbed in the planar case, so this scattering is not helping to increase the absorption by increasing the optical path.

When analyzing the contribution of different diffraction orders, we can see that the low energy diffraction orders with $g = 1$ have a bigger contribution to the spectrum up to 600 nm. One positive benefit is that lower energy diffraction orders have more robust diffraction efficiency than higher energy when introducing defects smaller than the lattice structures. For long wavelengths, the angle associated with $g = 1$, from 800 to 880 nm, is $\theta_d(g = 1)$ =31, 27°. This angle is responsible for the shifted FP resonance. However, this angle is not high enough to confine the light by itself inside the GaAs, as the angle for total internal reflection for the GaAs with the front TiO_2 is 42°. The front PC combines the anti-reflection strategy found in the literature, with

Optics EXPRESS

a tuned FP for long wavelengths. The higher peak for losses in the silver mirror is associated with the non-scattered FP resonances, but it is not with the scattered peaks, see Fig. 2(a).

The back PC non-scattered contribution for long wavelengths increases similarly to Beer-Lambert absorption without FP resonances. There is only one small peak that can be associated with a FP resonance. However, the non-scattered absorption dominates at shorter wavelengths, as the thickness and extinction coefficient of the GaAs is enough to absorb all the light. The scattered absorption is the more prominent contributor to the total absorption in the long wavelength regime. For long wavelengths in the Urbach tail, from 873 nm to 900 nm, we can see significant absorption and also that there is the only contribution from high energy orders with $g = 2$. The enhanced absorption is because the angle associated with this family of order is $\theta_d(g = 2) = 72°$ ($\lambda = 890$ nm). This angle is big enough to obtain total internal reflection for a light wave coming from the GaAs to the immediate next layer of TiO_2. Therefore, the incident light is coupled to a waveguide mode. This mode is the main contribution to the absorption until the extinction coefficient of the GaAs increases in the bandgap, and then the waveguide condition is not fundamental to increase the absorption. The contribution from the $g = 1$ (with an angle 30 °) also presents FP peaks, on top of the non-scattered contribution similarly to the front PC case. The family of orders with $g = \sqrt{2}$ has an angle of $\theta_d(g = \sqrt{2}) = 40°$. This angle is in the limit of being confined by total internal reflection. When combining both effects, the absorption reaches 98% at 843 nm. When the wavelength decreases the contribution of the non-scattered light also decreases. The back PC primarily contributes in the long wavelength region, as the front planar ARC takes care of the short wavelengths. The highest absorption peak in the silver mirror appears above 900 nm. Likewise, a peak appears in the scattered absorption of the GaAs at this wavelength, but the metal limits the absorption value.

The combination of back and front PC maximizes the scattered contribution to the absorption at short wavelengths from the front PC, with the long wavelengths for the back PC. The absorption reaches consistently higher values than the other two nanostructured cases. For the front and back PC case, the non-scattered light presents three FP resonances in the long wavelength region, as the front PC case. But, these FP resonances are less intense in the front and back nanostructured case than for the only front nanostructured, see Fig. 2(c). Also, the incident light is scattered by the two PC, and therefore the non-scattered contribution is minimized. The lattice parameter is higher in this case compared to the other two, which allows propagating orders with higher g, as can be seen in Fig. 2. However, there is no apparent wave-guiding at long wavelengths as the total internal reflection is frustrated by the top front photonic crystal. The light is scattered twice, increasing the probability of escaping light. As with the only back PC case, the highest absorption peak in the silver mirror appears at wavelengths above the bandgap, with an associated peak in the scattered contribution. In both cases, the contribution to the absorption above 900 nm is limited by the absorption of the metal layer.

4.2. Fields and Poynting vector analysis

The three nanostructures presented have higher absorption and J_{sc} than the reference, because of the improvement in the long wavelength range. However, as we can see from the analysis of the absorption for each g, the absorption and propagation present different behavior for each case, where the absorption is the final result. To understand the cause and limitations of this, we study the power localization and propagation within the layers. The structures are analyzed using E^2, W_S, W_{S_p}, and $W_{S_{np}}$. We also calculate $A(z)$ as a continuous function to localize the absorption peaks within the optical stack. We study the fields for wavelengths, which are peaks in the scattered contribution of the absorption. Because of the divergence from the planar case and its impact on improving the J_{sc} of the device. We analyze the three more representative peaks in the long wavelength region for the front PC, back PC, and front and back PC for 872 nm, 890 nm, and 866 nm, respectively (see Fig. 3).

Optics EXPRESS

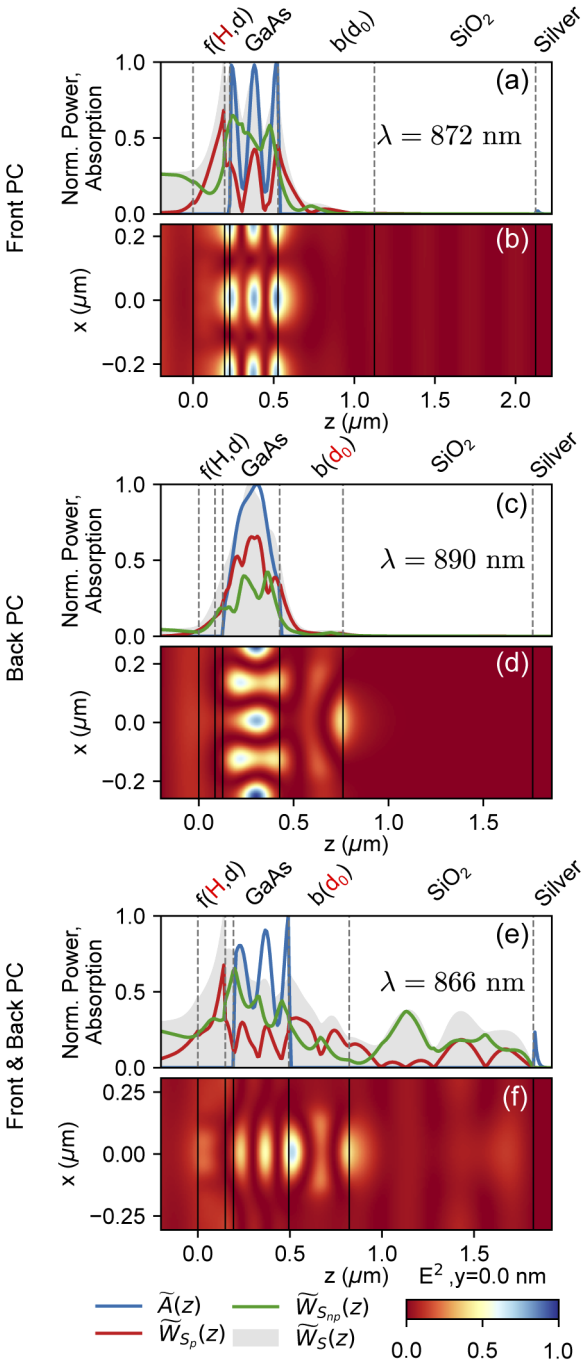

Fig. 3. Absorption (blue) and energies profiles, $\widetilde{W}_{S_{np}}$ (green) and $\widetilde{W}_{S_p}$ (red), the total $\widetilde{W}_S$, (gray filled) and E^2 for the front PC (a)-(b), back PC (c)-(d) and the front & back PC (e)-(f) respectively. The vertical dashed and thick lines represent the interfaces between the different materials layers following the design of Fig. 1(a). The layer thickness is highlighted in red when it is nanostructured for each case. The rest of modes for the front PC are shown in Visualization 1, for the back PC in Visualization 2, front and back PC in Visualization 3, and reference in Visualization 4.

Optics EXPRESS

Note that using W_S, W_{S_p}, and $W_{S_{np}}$, we have to be aware that we are calculating the power locally, without limiting the contribution to one incident planewave; namely, like with the E^2, we will have more power inside the structure when exciting one mode, than outside of it. In contrast, P limits the contribution to only one planewave, and the intensity it is always higher outside (initial power) than inside the cell, and decays after each absorption process.

The front PC at 872 nm presents a Fabry-Perot (FP) resonance with a small contribution from a waveguide mode. We can obtain this information by first analyzing the absorption profile inside the structure, with nodes across the GaAs slab. The profile agrees with the initial analysis from the scattered absorption. The structure is changing the propagation to an out of normal planewave. We can see also that the W_S, like the E^2, is concentrated in the GaAs slab. However, W_{S_p} is higher than $W_{S_{np}}$ in the front layer, the one containing the photonic crystal, but decays in the GaAs.

The back PC at 890 nm shows a waveguide mode coupled to the GaAs slab. The initial analysis just using the associated diffracted angle and the internal reflection predicted the possibility of coupling the incident light to this mode but without telling us the diffraction efficiency or where the mode is allowed to travel. We can see the power is concentrated in the GaAs slab by inspecting W_S and E^2, see in Figs. 3(c) and (d). The lattice parameter of the structure does not allow a diffracted order in the SiO_2 for normal incidence, the first order appears at 797 nm, helping to confine the light in the slab. The W_{S_p} contribution to this mode is over 50%, with an envelope in the amplitude of the mode profile. The high parallel contribution is responsible for the higher absorption in a region which typically does not have significant absorption with an extinction coefficient of $k = 0.0027$. The back PC layer acts like a *mirror*, with no power propagating through the SiO_2 or the silver mirror.

The front and back PC at 866 nm shows a different behavior to the other cases, not only because it is a shorter wavelength. The absorption profile presents an FP structure but reversed, meaning that the absorption is higher in the back part of the GaAs slab than in the front, see Fig. 3(e) blue line. This inverted absorption is counter-intuitive, as it is opposite to planar structures and simple Beer-Lambert law. We can understand this profile thanks to power analysis, E^2, and W_{S_p}. Inside the GaAs slab, the parallel component, W_{S_p}, is not following the decay of the W_S. Also, inside the back PC, we can see the major part of the contribution is parallel. We can associate this profile with a mode propagating in the back PC, close to interface with the GaAs slab. This increase in the parallel component creates this inverted profile in the absorption, as when the power mainly propagates parallel, the absorption increases.

In summary, the modes we have studied present three favorable cases to increase the absorption in the GaAs slab. First, a shifted FP resonance, which increases the absorption when the FP from the order zero is minimum, namely in anti-phase. Second, a waveguiding inside the GaAs thanks to the high scattering produced by the high index back PC and the internal reflection. Finally, the propagation of the light in the PC as localized modes in the PC layer and increasing the absorption by leaking to the GaAs slab. The front PC in the long-wavelength is dominated by the shifted FP resonances, whereas in the short wavelength, we can see some localized light in the PC. The back PC in the long-wavelength has a waveguide mode and localized light inside the PC. Whereas, the front and back PC increased absorption has a combination of FP resonances with PC localized light.

After the absorption and Poyinting analysis we can conclude that the front PC increased absorption mainly works by creating additional FP resonances. These resonances are out of phase respect the order zero FP resonance. In other words, the peaks and valleys of the scattered and and non-scattered light are in opposition, maximizing the total absorption. The FP resonance generated evenly distributes the absorption in nodes across the layer. Using a front PC can be used successfully when it is not possible to nanostructure in the rear of the cell, as in conventional monolithic multijunctions. But, creating this FP resonance has a cost on the final anti-reflection

Optics EXPRESS

properties of the nanostructure for shorter wavelengths. On the other hand, the back PC increased absorption appears because it can waveguide back the light in the upper layer, or increase the absorption in the immediate upper layer due to the localized light. It can be used to increase the absorption of ultrathin-single junction device, to thinner the bottom junction in monolithic devices, or for mechanically stacked tandems as III-V or perovskites on silicon as an interlayer. Combining both nanostructures increases the homogeneity of the absorption profile, and benefits from both effects.

5. Stability analysis

Real structures will have slightly varying parameters due to processing imperfections. We study the stability of the maxima obtained from the optimization. All the structures are defined by the optimized main variables, $x = a, R_f, R_b, H, d, d_0$ (The front PC assumes a $R_b = 0$, the back PC a $R_f = 0$). The variable space for these variables is too big to do a complete detailed map. Instead, we analyze two different random distributions, one uniform with a 30% variation (700 cases with 151 plane waves) for all the variables, and, a second one, using a Gaussian distribution with a $\sigma = 10\%$ for all the values except the lattice parameter with a $\sigma = 2\%$ (200 cases with 151 plane

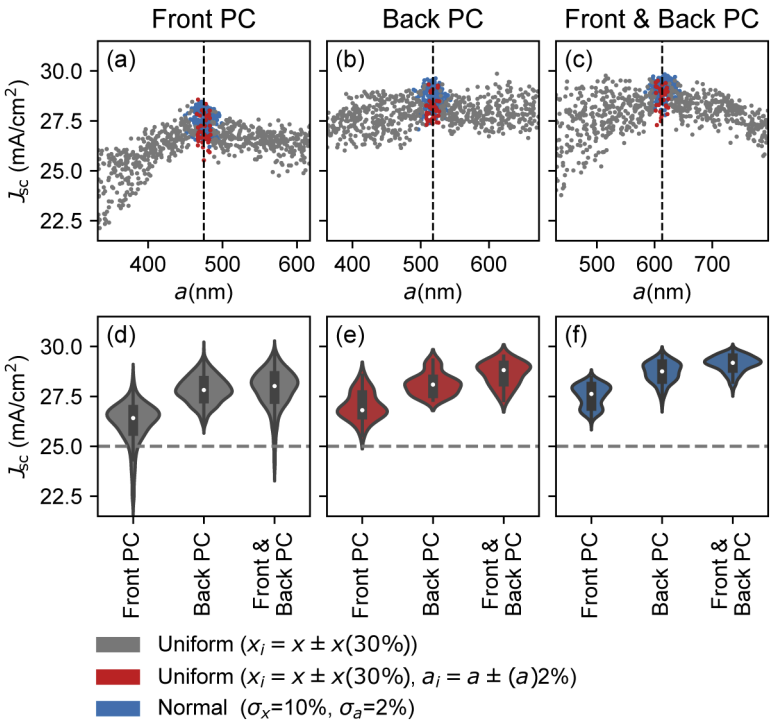

Fig. 4. Random structures around the optimum values (vertical black dashed line), showing the lattice parameter vs. the J_{sc}: for the front PC (a), back PC (b), and front and back PC (c). The gray dots correspond to an uniform distribution for structure size values ($x = a, R_f, R_b, H, d, d_0$) with ±30% variation, with an estimated probability density of the J_{sc}(d). The red dots are the subset of the uniform distribution limiting the variation in $a = a_i \pm 2\%$ with an estimated the probability density of the J_{sc} (e). The blue dots correspond with Gaussian distribution with $\sigma_x = 10\%$ for $x = R_f, R_b, H, d, d_0$ and $\sigma_a = 2\%$ with an estimated probability density of the J_{sc} (f). (d)-(f) The median is highlighted in white, and the thick black line are the second and third quartiles; the gray dashed lines represent the fixed planar case without nanostructures. The full data is available in Dataset 1 (Ref. [50]).

Optics EXPRESS

waves) emulating a fabrication. The J_{sc} distribution of these random structures are shown in Fig. 4 when compared to the lattice parameter, a, and summarize in Table 3. We do not add the photocurrent from the Urbach-tail. We estimate the probability density using a kernel density estimated without weights, see the violin plots Figs. 4(d)–(f) [48,49]. The uniform random distribution with $a \pm 30\%$ presents the highest deviation from the optimum. We expect this variation as it is essentially a brute optimization. However, the three nanostructured cases obtain as median values above the 25.0 mA/cm^2 of the reference. The higher J_{sc} is because even though the structures are not optimized, the materials chosen for the structures represent a reasonable starting point independently of the nanostructure geometry. The front PC is the more sensitive case as the structure is placed on the front. However, the median is slightly over the reference (26.2 mA/cm^2). The back PC presents a stable improvement with a distribution consistently above the reference, and a median higher than the reference (27.8 mA/cm^2). The Front and back PC presents a mixed tendency with a median comparable to the back PC, but with some structures failing behind the reference, see Fig. 4(d). The lattice parameter, a, dominates the maximum that can be obtained, especially for the structures with a front PC (see Figs. 4(a) and (c)). This correlation appears because a defines the diffraction orders available for the structure. The diffraction orders depend on the materials used, which are constant for all the random structures.

Table 3. Mean, ($\overline{J_{sc}}$), median, $M(J_{sc})$, and standard deviation, $\sigma_{J_{sc}}$, for the three nanostructured cases using three random distributions: an uniform distribution with a variation of ± 30% around the optimum value, a subset of the uniform distribution fixing the a to a variation of ± 2%, and a simulated fabrication with a normal distribution with σ = 10% for all the values except the σ_a = 2%.

Structure/Distribution	$\overline{J_{sc}}$(mA/cm^2)	$M(J_{sc})$(mA/cm^2)	$\sigma_{J_{sc}}$ (mA/cm^2)
Front PC			
Uniform ([$x \pm (30\%)$])	26.2	26.4	1.0
Uniform ([$x_i \pm (30\%)$], [$a \pm (2\%)$]	27.0	26.8	0.7
Normal (σ_{x_i}=10%, σ_a=2%)	27.5	27.6	0.6
Back PC			
Uniform ([$x \pm (30\%)$])	27.8	27.8	0.7
Uniform ([$x_i \pm (30\%)$], [$a \pm (2\%)$]	28.1	28.1	0.6
Normal (σ_{x_i}=10%, σ_a=2%)	28.7	28.8	0.5
Front and Back PC			
Uniform ([$x \pm (30\%)$])	27.9	28.0	1.0
Uniform ([$x_i \pm (30\%)$], [$a \pm (2\%)$]	28.6	28.8	0.6
Normal (σ_{x_i}=10%, σ_a=2%)	29.1	29.2	0.4

Not all the parameters have the same accuracy when doing a fabrication process. In particular, a is typically the more precise parameter in fabrication using nano-imprint or laser interference lithography. After all, nano-imprint uses a fixed mask pattern, and laser interference lithography uses a fixed laser wavelength and geometry. The other parameters as H, d, d_0, R_F and R_B are very dependant on the process used, deposition and/or etching techniques, [17,19,30] and therefore it is expected more fabrication difficulties. We narrow the uniform distribution to only the structures with a lattice parameter within a ±2% of the optimum value, see Figs. 4(a)–(c) red dots, and Fig. 4(e). These variations in the lattice are roughly 10 nm. By only narrowing the a, we limit all the outliers present and modify the estimated density plot, Fig. 4(e), especially for the structures with a front PC. The only back PC structure presents a small improvement, as it is the more robust structure under lattice parameter changes. We can see that the median for structures with a front and back PC obtain J_{sc} 28.8 mA/cm^2, Table 3. These front and back PC structures share the lattice parameter and the materials, which play a decisive role in the final performance.

Optics EXPRESS

Furthermore, the back PC structures present a higher J_{sc} and lower standard deviation than the front PC, see Table 3.

Finally we emulate a fabrication process by assuming a Gaussian distribution with a standard deviation (σ) of σ_x=10% of the optimized value for $x = H, R_f, R_b, d, d_0$ and a σ_a =2% for the lattice parameter, see Figs. 4(a)-(c) and (f). The more sensitive structure is still the only a front PC, with a $\sigma_{J_{sc}}$= 0.6 mA/cm^2, (2.2% of the mean value). The back PC structure improves the median value, as we can see also from comparing the probability density (Figs. 4(d),(e) vs. (f)). The front and back PC J_{sc} median and mean obtains the highest value, whereas it presents the lower σ. This is clear from the estimated probability density in Fig. 4(f). The additional structure improves the stability compared to the single layer PC structures with a lower σ.

In summary, the stability of the structures with a back PC is higher than the structure with only one front PC. The structures with a back PC shows $\sigma \approx 0.5$mA/cm^2. However, the front and back PC present the highest mean for the J_{sc}, and lower σ despite the added complexity of the structure.

6. Conclusions

We present an optimized strategy to obtain optically effectively thick structures with just 300 nm of GaAs absorber using front and back photonic crystals outside of the cell. We use nanostructured layers surrounding the solar cell, made of transparent materials for the useful spectrum: a transparent dielectric for the front nanostructure (TiO_2) and high band-gap semiconductors (AlGaAs) for the back of the cell. We use AlGaAs because of its high index but transparency tunability with the Al composition. Also, we add a dielectric spacer between the nanostructured layers in the back of the cell and the back metallic mirror, to minimize the absorption in the metal. We predict a maximum J_{sc} of 29.6 mA/cm^2 when using 300 nm GaAs absorber, dual PC layers, and a nominal bandgap of 1.42 eV. Also, when we included the sub-bandgap absorption, we obtain a maximum of 29.9 mA/cm^2. Both values are comparable to a thick absorber of 3μm one order of magnitude thicker. Furthermore, we study the absorption by splitting the contributions of the scattered and non-scattered light. This way, we can identify the absorption enhanced by each layer with photonic crystals and isolated from the typical Fabry-Perot and Beer-Lambert absorption profiles. Using the maxima of the scattered contribution, we study the propagation inside the structure identifying the power propagation with the norm of the parallel component of the Poynting vector. The structures presented benefits from increased absorption: by using Fabry-Perot resonances for the diffracted light, coupling the normal incidence light to waveguide modes inside the GaAs layer, and by having propagating localized light (modes) inside the photonic crystals and then increasing the absorption to the upper layer. The absorption is enhanced where is mostly needed for a thin device, long wavelengths close to the bandgap.

Funding

U.S. Department of Energy (DE-AC36-08GO28308), by the National Renewable Energy Laboratory, operated by Alliance for Sustainable Energy, LLC; Office of Energy Efficiency and Renewable Energy; Solar Energy Technologies Office (34358, 34911).

Acknowledgments

The authors thanks Mark Steger, Bill E. McMahon, Jose M. Llorens and John F. Geisz for the helpful discussions. This research was performed using computational resources sponsored by the Department of Energy's Office of Energy Efficiency and Renewable Energy and located at the National Renewable Energy Laboratory. The views expressed in the article do not necessarily represent the views of the DOE or the U.S. Government.

Optics EXPRESS

Disclosures

The authors declare no conflicts of interest.

References

1. M. A. Green, Y. Hishikawa, E. D. Dunlop, D. H. Levi, J. Hohl-Ebinger, M. Yoshita, and A. W. Y. Ho-Baillie, "Solar cell efficiency tables (Version 53)," Prog. Photovoltaics **27**(1), 3–12 (2019).
2. R. Fu, D. Feldman, and R. Margolis, "U.S. Solar Photovoltaic System Cost Benchmark: Q1 2018," *Renewable Energy* p. 63 (2018).
3. A. Richter, M. Hermle, and S. W. Glunz, "Reassessment of the Limiting Efficiency for Crystalline Silicon Solar Cells," IEEE J. Photovoltaics **3**(4), 1184–1191 (2013).
4. I. Almansouri, A. Ho-Baillie, S. P. Bremner, and M. A. Green, "Supercharging Silicon Solar Cell Performance by Means of Multijunction Concept," IEEE J. Photovoltaics **5**(3), 968–976 (2015).
5. D. C. Bobela, L. Gedvilas, M. Woodhouse, K. A. W. Horowitz, and P. A. Basore, "Economic competitiveness of III –V on silicon tandem one-sun photovoltaic solar modules in favorable future scenarios," Prog. Photovoltaics **25**(1), 41–48 (2016).
6. T. Leijtens, K. A. Bush, R. Prasanna, and M. D. McGehee, "Opportunities and challenges for tandem solar cells using metal halide perovskite semiconductors," Nat. Energy **3**(10), 828–838 (2018).
7. K. A. Horowitz, T. W. Remo, B. Smith, and A. J. O. Ptak, A Techno-Economic Analysis and Cost Reduction Roadmap for III-V Solar Cells, Tech. Rep. NREL/TP-6A20-72103, National Renewable Energy Lab. (NREL), Golden, CO (United States) (2018).
8. M. Yamaguchi, "Radiation-resistant solar cells for space use," Sol. Energy Mater. Sol. Cells **68**(1), 31–53 (2001).
9. L. C. Hirst, M. K. Yakes, J. H. Warner, M. F. Bennett, K. J. Schmieder, R. J. Walters, and P. P. Jenkins, "Intrinsic radiation tolerance of ultra-thin GaAs solar cells," Appl. Phys. Lett. **109**(3), 033908 (2016).
10. A. Mellor, N. Hylton, S. Maier, and N. Ekins-Daukes, "Interstitial light-trapping design for multi-junction solar cells," Sol. Energy Mater. Sol. Cells **159**, 212–218 (2017).
11. P. Dutta, M. Rathi, P. Ahrenkiel, Y. Gao, A. Mehrotra, E. Galstyan, M. Iliev, B. Makarenko, R. Forrest, A. Freundlich, and V. Selvamanickam, "Epitaxial thin film GaAs deposited by MOCVD on low-cost, flexible substrates for high efficiency photovoltaics," in *2013 IEEE 39th Photovoltaic Specialists Conference (PVSC)*, (2013), pp. 3393–3396.
12. A. Mehrotra, W. Wang, and A. Freundlich, "Modeling and fabrication of GaAs solar cells with high dislocation tolerance," in *2014 IEEE 40th Photovoltaic Specialist Conference (PVSC)* (2014), pp. 0514–0519.
13. Y. Alaskar, S. Arafin, D. Wickramaratne, M. A. Zurbuchen, L. He, J. McKay, Q. Lin, M. S. Goorsky, R. K. Lake, and K. L. Wang, "Towards van der Waals Epitaxial Growth of GaAs on Si using a Graphene Buffer Layer," Adv. Funct. Mater. **24**(42), 6629–6638 (2014).
14. W. Yang, J. Becker, S. Liu, Y.-S. Kuo, J.-J. Li, B. Landini, K. Campman, and Y.-H. Zhang, "Ultra-thin GaAs single-junction solar cells integrated with a reflective back scattering layer," J. Appl. Phys. **115**(20), 203105 (2014).
15. D. Liang, Y. Kang, Y. Huo, Y. Chen, Y. Cui, and J. S. Harris, "High-Efficiency Nanostructured Window GaAs Solar Cells," Nano Lett. **13**(10), 4850–4856 (2013).
16. S.-M. Lee, A. Kwong, D. Jung, J. Faucher, R. Biswas, L. Shen, D. Kang, M. L. Lee, and J. Yoon, "High Performance Ultrathin GaAs Solar Cells Enabled with Heterogeneously Integrated Dielectric Periodic Nanostructures," ACS Nano **9**(10), 10356–10365 (2015).
17. H.-L. Chen, A. Cattoni, R. D. Lépinau, A. W. Walker, O. Höhn, D. Lackner, G. Siefer, M. Faustini, N. Vandamme, J. Goffard, B. Behaghel, C. Dupuis, N. Bardou, F. Dimroth, and S. Collin, "A 19.9%-efficient ultrathin solar cell based on a 205-nm-thick GaAs absorber and a silver nanostructured back mirror," Nat. Energy **4**(9), 761–767 (2019).
18. J. Xiao, H. Fang, R. Su, K. Li, J. Song, T. F. Krauss, J. Li, and E. R. Martins, "Paths to light trapping in thin film GaAs solar cells," Opt. Express **26**(6), A341–A351 (2018).
19. J. Tommila, A. Aho, A. Tukiainen, V. Polojärvi, J. Salmi, T. Niemi, and M. Guina, "Moth-eye antireflection coating fabricated by nanoimprint lithography on 1 eV dilute nitride solar cell," Prog. Photovoltaics **21**, 1158–1162 (2012).
20. N. Gruginskie, S. C. W. van Laar, G. Bauhuis, P. Mulder, M. van Eerden, E. Vlieg, and J. J. Schermer, "Increased performance of thin-film GaAs solar cells by rear contact/mirror patterning," Thin Solid Films **660**, 10–18 (2018).
21. J. Buencuerpo, J. M. Llorens, M. L. Dotor, and J. M. Ripalda, "Photon management with nanostructures on concentrator solar cells," Appl. Phys. Lett. **103**(8), 083901 (2013).
22. J. Buencuerpo, J. F. Geisz, M. A. Steiner, and A. C. Tamboli, "Enabling ultrathin III-V solar cells using dual photonic crystals," in *2019 IEEE 46th Photovoltaic Specialists Conference (PVSC)* (IEEE, Chicago IL, 2019).
23. D. Eisenhauer, G. Köppel, K. Jäger, D. Chen, O. Shargaieva, P. Sonntag, D. Amkreutz, B. Rech, and C. Becker, "Smooth anti-reflective three-dimensional textures for liquid phase crystallized silicon thin-film solar cells on glass," Sci. Rep. **7**(1), 2658–2710 (2017).
24. O. Isabella, H. Sai, M. Kondo, and M. Zeman, "Full-wave optoelectrical modeling of optimized flattened light-scattering substrate for high efficiency thin-film silicon solar cells," Prog. Photovoltaics **22**(6), 671–689 (2014).
25. A. Bozzola, M. Liscidini, and L. C. Andreani, "Broadband light trapping with disordered photonic structures in thin-film silicon solar cells," Prog. Photovoltaics **22**, 1237–1245 (2013).
26. M. A. Green, "Lambertian light trapping in textured solar cells and light-emitting diodes: Analytical solutions," Prog. Photovoltaics **10**(4), 235–241 (2002).

Optics EXPRESS

27. M. van Eerden, G. J. Bauhuis, P. Mulder, N. Gruginskie, M. Passoni, L. C. Andreani, E. Vlieg, and J. J. Schermer, "A facile light-trapping approach for ultrathin GaAs solar cells using wet chemical etching," Prog. Photovoltaics **28**(3), 200–209 (2020).
28. E. Kretschmann and H. Raether, "Notizen: Radiative Decay of Non Radiative Surface Plasmons Excited by Light," Z. Naturforsch., A: Phys. Sci. **23**(12), 2135 (2014).
29. A. Otto, "Excitation of nonradiative surface plasma waves in silver by the method of frustrated total reflection," Z. Phys. A: Hadrons Nucl. **216**(4), 398–410 (1968).
30. J. Buencuerpo, L. Torné, R. Álvaro, J. M. Llorens, M. L. Dotor, and J. M. Ripalda, "Nano-cones for broadband light coupling to high index substrates," Sci. Rep. **6**(1), 38682 (2016).
31. J. Buencuerpo, J. M. Llorens, M. L. Dotor, and J. M. Ripalda, "Broadband antireflective nano-cones for tandem solar cells," Opt. Express **23**(7), A322 (2015).
32. E. E. Perl, W. E. McMahon, R. M. Farrell, S. P. DenBaars, J. S. Speck, and J. E. Bowers, "Surface Structured Optical Coatings with Near-Perfect Broadband and Wide-Angle Antireflective Properties," Nano Lett. **14**(10), 5960–5964 (2014).
33. S. G. Johnson, The NLopt nonlinear-optimization package, http://github.com/stevengj/nlopt.
34. P. Kaelo and M. M. Ali, "Some Variants of the Controlled Random Search Algorithm for Global Optimization," J Optim Theory Appl **130**(2), 253–264 (2006).
35. M. J. D. Powell, "Direct search algorithms for optimization calculations," Acta Numerica **7**, 287–336 (1998).
36. V. Liu and S. Fan, "S4 : A free electromagnetic solver for layered periodic structures," Comput. Phys. Commun. **183**(10), 2233–2244 (2012).
37. S. Babar and J. H. Weaver, "Optical constants of Cu, Ag, and Au revisited," Appl. Opt. **54**(3), 477–481 (2015).
38. S. Tanemura, L. Miao, P. Jin, K. Kaneko, A. Terai, and N. Nabatova-Gabain, "Optical properties of polycrystalline and epitaxial anatase and rutile TiO2 thin films by rf magnetron sputtering," Appl. Surf. Sci. **212-213**, 654–660 (2003).
39. D. E. Aspnes, S. M. Kelso, R. A. Logan, and R. Bhat, "Optical properties of AlxGa1-x As," J. Appl. Phys. **60**(2), 754–767 (1986).
40. E. D. Palik, *Handbook of Optical Constants of Solids II* (Academic Press, 1991).
41. S. G. Tikhodeev, A. L. Yablonskii, E. A. Muljarov, N. A. Gippius, and T. Ishihara, "Quasiguided modes and optical properties of photonic crystal slabs," Phys. Rev. B **66**(4), 045102 (2002).
42. S. Fan and J. D. Joannopoulos, "Analysis of guided resonances in photonic crystal slabs," Phys. Rev. B **65**(23), 235112 (2002).
43. J. Song, R. P. Zaccaria, M. B. Yu, and X. W. Sun, "Tunable Fano resonance in photonic crystal slabs," Opt. Express **14**(19), 8812–8826 (2006).
44. P. Feynman Richard, *The Feynman Lectures on Physics*, Vol. II Imperial College Press, (2017).
45. J. Nelson, *The Physics of Solar Cells*, 1st ed (Imperial College Press, 2003).
46. A. Mellor, I. Tobías, A. Martí, M. Mendes, and A. Luque, "Upper limits to absorption enhancement in thick solar cells using diffraction gratings," Prog. Photovoltaicsx **19**(6), 676–687 (2011).
47. D. Ding, S. R. Johnson, S.-Q. Yu, S.-N. Wu, and Y.-H. Zhang, "A semi-analytical model for semiconductor solar cells," J. Appl. Phys. **110**(12), 123104 (2011).
48. D. W. Scott, *Multivariate Density Estimation: Theory, Practice, and Visualization*, 1st ed (Wiley, New York, 1992).
49. M. Waskom, O. Botvinnik, J. Ostblom, S. Lukauskas, P. Hobson MaozGelbart, D. C. Gemperline, T. Augspurger, Y. Halchenko, J. B. Cole, J. Warmenhoven Julian de Ruiter, C. Pye, S. Hoyer, J. Vanderplas, S. Villalba, G. Kunter, E. Quintero, P. Bachant, M. Martin, K. Meyer, C. Swain, A. Miles, T. Brunner, D. O'Kane, T. Yarkoni, M. L. Williams, and C. Evans, "Mwaskom/seaborn: V0.10.0 (January 2020), Zenodo," (2011).
50. J. Buencuerpo, M. A. Steiner, and A. C. Tamboli, Photocurrent stability study for a 300 nm nanostructured GaAs cell around the maximum, figshare (2020)[retrieved 9 April 2020. https://doi.org/10.6084/m9.figshare.12104046.